The phase diagrams of beryllium and magnesium oxide at megabar pressures

Jizhou Wu

Department of Earth and Planetary Science, University of California, Berkeley, CA 94720, USA

E-mail: `wjz8597@berkeley.edu`

Felipe González-Cataldo

Department of Earth and Planetary Science, University of California, Berkeley, CA 94720, USA

E-mail: `f_gonzalez@berkeley.edu`

François Soubiran

CEA DAM-DIF, 91297 Arpajon, France

E-mail: `Francois.SOUBIRAN@cea.fr`

Burkhard Militzer

Department of Earth and Planetary Science, University of California, Berkeley, CA 94720, USA
Department of Astronomy, University of California, Berkeley, CA 94720, USA

E-mail: `militzer@berkeley.edu`

Abstract. We perform *ab initio* simulations of beryllium (Be) and magnesium oxide (MgO) at megabar pressures and compare their structural and thermodynamic properties. We make a detailed comparison of our two recently derived phase diagrams of Be [Wu *et al.*, Phys. Rev. B **104**, 014103 (2021)] and MgO [Soubiran and Militzer, Phys. Rev. Lett. **125**, 175701 (2020)] using the thermodynamic integration technique, as they exhibit striking similarities regarding their shape. We explore whether the Lindemann criterion can explain the melting temperatures of these materials through the calculation of the Debye temperature at high pressure. From our free energy calculations, we **find that the melting line of both materials is well represented by the Simon-Glazel fit $T_m(P) = T_0(1+P/a)^{1/c}$, where $T_0 = 1564$ K, $a = 15.8037$ GPa and $c = 2.4154$ for Be, while $T_0 = 3010$ K, $a = 10.5797$ GPa and $c = 2.8683$ for the MgO in the B1. For the B2 phase, we use the values $a = 26.1163$ GPa and $c = 2.2426$.** Both materials exhibit negative Clapeyron slopes on the boundaries between the two solid phases that are strongly affected by anharmonic effects, which also influence the location of the solid-solid-liquid triple point. We find that the quasi-harmonic approximation underestimates the stability range of the low-pressure phases, namely hcp for Be and B1 for MgO. We also compute the phonon dispersion relations at low and high pressure for each of the phases of these materials, and also explore how the phonon density of states is modified by temperature. Finally, we derive secondary shock Hugoniot curves in addition to the principal Hugoniot curve for both materials, and study their offsets in pressure between solid and liquid branches.

1. Introduction

Phase transitions are ubiquitous and significant in many areas of scientific research including condensed matter physics, geophysics, and planetary science [1, 2, 3]. Pressure-induced phase transitions, in particular, modify the crystalline structure and thermodynamic properties of a material and are thus crucial to characterize planetary interiors [4, 5, 6, 7, 8, 9, 10]. Different crystalline phases of the same material can have substantially different optical properties and elastic responses, which affects how sound waves or seismic waves propagate. Knowing the exact location of phase boundaries is also relevant for the interpretation of shock experiments that are able to compress materials to high pressures and temperatures. Magnesium oxide (MgO) is part of the ferropericlase mineral family and one of the major building blocks of the Earth's mantle. It is also assumed to be a major component of rocky exoplanets, playing an important role in the rheology and stratification of large exoplanets with mantles under pressures much higher than those present at the Earth interior [11]. **In high-pressure experiments, MgO is also used as a pressure standard because its equation of state at low temperatures is well established [12, 13, 14]. Moreover, MgO is also commonly used in metallurgy as well as in the environmental and construction industry as a refractory material because of its high thermal conductivity and low electrical conductivity [15, 16].** MgO has an NaCl-type (B1) structure at low pressures that transforms into a CsCl-type structure (B2) at approximately 400-600 GPa [17] and this B1-B2 transition can affect the heat flow and thermal evolution of rocky exoplanets [18, 19, 20, 11].

Beryllium **is used in plasma physics, nuclear science, and space science, being the main component of the low-weight mirrors of the recently launched James Webb Space Telescope [21].** It exhibits a phase diagram at megabar pressures that very much resembles that of MgO: it has an hcp phase that transforms to a bcc phase at high pressure. The latter is equivalent to the B2 phase of MgO if the atoms were of the same species (see Fig. 1). In fact, pure Mg, which is in the same group as Be in the periodic table, also exhibits an hcp to bcc transition, but at much lower pressures [22].

There have been many attempts to calculate the high pressure solid-solid boundary in the phase diagram of MgO [17, 23, 24, 25, 26, 27, 28, 29] and Be [30, 31, 32, 33, 34]. Most of them rely on the quasi-harmonic approximation (QHA), in which the free energy is calculated from volume-dependent phonons and a decoupled electronic contributions. This approximation breaks down at high temperature where anharmonic effects can play an important role [35, 17, 24, 33]. Several experiments have been performed to observe the high pressure phases of both materials but bcc phase of beryllium has not been detected neither in laser-heated diamond anvil cell [36] nor with shock compression experiments [37]. It was concluded that the low-pressure phases are much more stable than the QHA had predicted [36, 37]. B1-B2 solid phase transition in MgO has been observed in recent ramp compression experiments [11]. Temperature measurements, however, are still lacking, making it difficult to establish the exact location of the B1-B2 phase boundary.

In this study, we use *ab initio* simulations to derive thermodynamic and vibrational properties of MgO and Be at high pressure. We compare the phase diagrams of these materials that we have derived from free energy calculations [17, 35], discussing the similarities between them, and analyze how anharmonic effects modify the phase boundaries at high temperature. We also use the equation of state that we have generated to derive secondary shock Hugoniots curves that depart from principal Hugoniot curve and make predictions where double-shock compression experiments would intersect the melting line. We also compare the phonon dispersion relationships and show how they change with pressure and temperature for each phase, offering a tentative explanation for anharmonic effects that are common to both phase diagrams.

2. Methods

2.1. Density functional molecular dynamics

We performed Kohn-Sham density functional molecular dynamics (DFT-MD) simulations using the Vienna Ab initio Simulation Package (VASP) [38] under the projector augmented wave [39, 40] method and a canonical ensemble regulated with a Nosé-Hoover thermostat [41, 42]. The Mermin functional [43] was used throughout to incorporate the effects of excited electronic states at elevated temperatures. The exchange-correlation effects were modeled with the Perdew–Burke–Ernzerhof (PBE) functional in generalized gradient approximation (GGA) [44]. The $1s^22s^2$ electrons were treated as valence configuration in the simulations of Be, while $1s^2$ frozen cores of magnesium and oxygen were used leaving 10 and 6 electrons as valence, respectively [45, 46]. Electronic orbitals are expanded in a plane-wave basis with an energy cut-off of 1,000 eV for Be and 1,200 eV for MgO. We chose a time step of 1.0 fs and total simulation times of at least 2 ps to average the thermodynamic quantities. The error bars were derived from blocking method [47, 48]. We use a Monkhorst-Pack grid [49] of $2 \times 2 \times 2$ k-points to sample the Brillouin zone in our MD simulations of

Be, of Γ point only for MgO. A k-point correction to the DFT-MD results of Be has been applied in order to correct for the insufficient sampling of the Brillouin zone [35].

Molecular dynamics simulations of Be were performed in 128- ($4 \times 4 \times 4$) and 144-atoms ($4 \times 3 \times 3$) orthorhombic supercells for bcc and hcp phases, respectively. For MgO, we chose a 64-atom supercell for the B1 phase and 250 atoms for the B2 phase. Liquid simulations were performed in cubic cells with 128 atoms for Be and 64 atoms for MgO. Finite size effects were analyzed and found to be small in our previous publications [17, 35].

2.2. Thermodynamic Integration

In order to calculate the Gibbs free energy of each system, we employed the thermodynamic integration method [50, 51, 52, 53] that allows one to derive as the Helmholtz free energy of solid and liquid phases. For a solid structure governed by DFT forces, we use the expression

$$F_{\mathrm{DFT}} = F_{\mathrm{Ein}} + \Delta F_{\mathrm{Ein} \to \mathrm{cl}} + \Delta F_{\mathrm{cl} \to \mathrm{DFT}}, \qquad (1)$$

where F_{Ein} is the Helmholtz free energy of an Einstein crystal of the same density. The second term represents the free energy difference between an Einstein crystal and a solid system ruled by a classical potential. The last term is free energy difference between that classical system and the DFT system of interest, where the interactions are controlled by the Kohn-Sham equations. These free energy differences are calculated at fixed volume and temperature using the thermodynamic integral

$$\Delta F_{a \to b} = F_b - F_a = \int_0^1 d\lambda \ \langle U_{\mathrm{b}}(r_i) - U_{\mathrm{a}}(r_i) \rangle_\lambda, \qquad (2)$$

where the brackets represent an ensemble average for a system ruled by the hybrid potential $U(\lambda) = (1 - \lambda)U_a + \lambda U_b$. This defines a continuous transformation between two systems governed by the potential energies U_a and U_b.

The classical system is controlled by a combination of harmonic and pair forces, which are fitted to match the DFT forces along MD trajectory [54, 55, 56, 57]. The construct five λ-ensembles to evaluate the term, $\Delta F_{\mathrm{cl} \to \mathrm{DFT}}$ are generated with molecular dynamics simulations because they allow for efficient propagation of electronic wave functions. The evaluation of the $\Delta F_{\mathrm{Ein} \to \mathrm{cl}}$ requires very little computer time in comparison and is evaluated with Monte Carlo methods using fifty or more λ steps. When the system analyzed is a liquid, we change F_{Ein} by F_{ig}, the free energy of an ideal gas.

We do not apply the Frenkel correction to the free energy of solid phases [50, 58] because it overestimates

the correction that results from fixing the center of mass in the simulations [53], introducing additional finite size effects that lead to an incorrect predictions for the melting temperature [17, 35].

2.3. Quasi-harmonic approximation and phonon quasi-particle method

We performed a number of phonon calculations under the quasi-harmonic approximation using density-functional perturbation theory (DFPT) [59] and the PHONOPY software [60]. In QHA, the free energy of the system is decomposed into three terms

$$F(V,T) = E_0(V) + F_e(V,T) + F_i(V,T), \qquad (3)$$

where E_0 is the internal energy of perfect lattice, F_e is the electronic contribution of free energy obtained from the Mermin functional [43], and F_i is the harmonic vibrational free energy of the lattice, calculated from eigenvalues of dynamical matrix from DFPT simulation. We ignored the electronic excitation term since it accounts for no more than 2% of total free energy [35].

Harmonic phonon frequencies were computed with DFPT and we found that $4 \times 4 \times 4$ supercells containing 128 atoms for Be in the hcp phase were sufficiently large to yield accurate phonon dispersion relationships. We used 64 atoms for Be in the bcc phase and 128 atoms for MgO in the B1 and B2 phases. The Brillouin zone was sampled with a Γ-centered grid of $3 \times 3 \times 3$ k-points for Be and MgO. In addition, we also used the DYNAPHOPY software [61] to obtain the frequencies and lifetimes of the phonon quasiparticles, which are temperature dependent [35, 33, 61, 62] from the velocity autocorrelation function in our DFT-MD simulations:

$$G_{\mathbf{q}s}(\omega) = \int_0^{+\infty} \langle V_{\mathbf{q}s}(0) V_{\mathbf{q}s}(t) \rangle e^{i\omega t} \, dt. \qquad (4)$$

Here, $\mathbf{q}$ is the wave vector in Brillouin zone, s is the index of the phonon branch and $V_{\mathbf{q}}(t) = \sum_{i=1}^N \sqrt{m_i} \exp{(i\mathbf{q} \cdot \mathbf{R}_i)} \mathbf{v}_i(t) \cdot \mathbf{e}_{qs}^i$ is mass-weighted and projected velocity for a normal mode $(\mathbf{q}, s)$ [33] at a given time t of our DFT-MD trajectory. Here, m_i and R_i represent the mass and equilibrium coordinate of the atom i, and $\mathbf{e}_{qs}^i$ is the phonon polarization vector obatined from lattice dynamics [33, 62, 63].

3. Results and discussion

3.1. Phase diagrams of MgO and Be

Using the thermodynamic integration method, we recently derived the high pressure phase diagrams of MgO [17] and Be [35]. Despite the very different nature of both systems, their phase diagrams exhibit striking similarities as can be seen in Fig. 1. Both Be and MgO
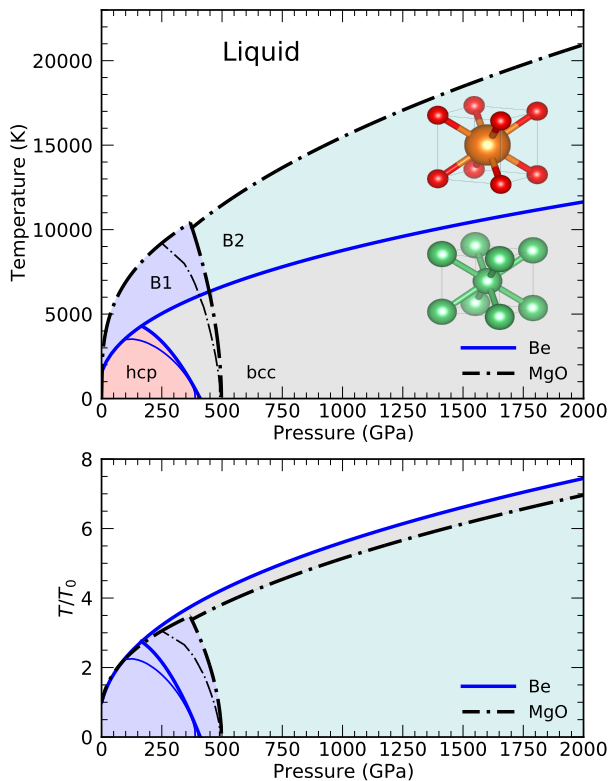
Figure 1. Overlay of the phase diagrams of MgO and Be. The upper dash-dotted lines indicate the boundaries between B1, B2, and liquid phase of MgO. The lower solid lines show the boundaries between hcp, bcc, and liquid phases of Be. The upper inset shows the B2 structure, in which the O atom occupy positions in the corner on a body-centered cubic (bcc) lattice, and Mg in the center. Below, the unit cell of Be in the bcc phase is shown with green spheres. All thick phase boundaries were calculated with the thermodynamic integration method [17, 35]. The thin lines correspond to calculations using the QHA method [23, 31].

have a negative Clapeyron slope along the solid-solid phase boundary, and a positive slope along the melting curve, which renders both phase diagram rather similar in the pressure regime under consideration. Both phase diagrams include a triple point located at 370 GPa and 10 000 K for MgO and 165 GPa and 4314 K for Be. We attribute this difference in temperature and pressure to the fact that MgO is governed by ionic bonds that are stronger than the metallic bonds in Be.

It has been shown that the quasi-harmonic approximation underestimates the thermodynamic stability range of the low-pressure phases [17, 35], namely hcp for Be and B1 for MgO, because it relies exclusively on harmonic phonon frequencies calculated for a static lattice ($T = 0$ K). When anharmonic contributions are included the boundary between solid phases but also the triple points of MgO and Be shift towards higher pressures.

The low-pressure phases of MgO and Be have

been seen in multiple high pressure experiments but only a recent study by Coppari *el al.* [64] confirmed the existence of the B2 phase of MgO with X-ray diffraction measurements. The bcc phase of Be has not yet been confirmed with experiments [36, 37].

3.2. Melting curves and validity of Lindemann's law

The Lindemann melting criteria predicts that melting of a solid occurs if the root mean squared displacement (rMSD) of the atoms, $\sqrt{\langle u^2 \rangle}$, reaches a certain fraction of the nearest neighbor distance, a. It has been used to predict the melting curves of materials [65] as a simple alternative to other methods that predict melting temperatures [66]. If one derives $\sqrt{\langle u^2 \rangle}$ within harmonic theory [67, 68, 69, 70, 71, 72], this fraction, f, can be expressed in terms of the Debye temperature, Θ_D, [69, 70]

$$f^2 \equiv \frac{\langle u^2 \rangle}{a^2} \approx \frac{9\hbar^2 T_m}{\overline{M} k_B a^2 \Theta_D^2} \equiv \frac{T_m}{T_*}, \qquad (5)$$

where T_m denotes the melting temperature, $\overline{M}$ the average mass, and $\hbar$ and k_{B} are Plank and Boltzmann constants, respectively. **The melting temperatures of both materials are well represented by the Simon-Glazel fit $T_m(P) = T_0(1 + P/a)^{1/c}$. The melting line of both Be phases can be approximate by $T_0 = 1564$ K, $a = 15.8037$ GPa, and $c = 2.4154$. For MgO, we employ a common T_0 value of 3010 K and represent the B1 melting line by $a = 10.5797$ GPa and $c = 2.8683$ and the B2 melt curve by $a = 26.1163$ GPa and $c = 2.2426$ [17, 35]. When the melting temperature is normalized by T_0 in Fig. 1, one notices that the melting lines of MgO and Be are very similar. At 2000 GPa, the melting temperatures are 7.0 and 7.5 times as high as their respective ambient values. In the limit of $P \gg a$, one finds $T_m/T_0 \approx (P/a)^{1/c}$, which leads to a similar high-pressure behavior for both materials.**

For convenience, we have introduced $T_* \equiv \overline{M} k_B a^2 \Theta_D^2 / 9\hbar^2$ as a normalizing factor for the melting temperatures. For a number of materials, the value of f at ambient pressure has been estimated to lie between 9% and 19% [70], but it can reach values as high as 27% for light elements such as hydrogen [73]. If the interaction between atoms is purely repulsive, the value of f is expected to remain constant along the melting line for monatomic systems [74], which would in principle offer a very simple way to predict the melting line of a material because only the rMSD is needed for different P and T conditions.

Debye temperature can be expressed in terms of logarithmic phonon moment: [30],

$$\Theta_D \equiv \frac{\hbar}{k_B} \exp\left(\frac{1}{3} + \int_0^\infty g(\omega) \ln(\omega)\, d\omega\right), \qquad (6)$$
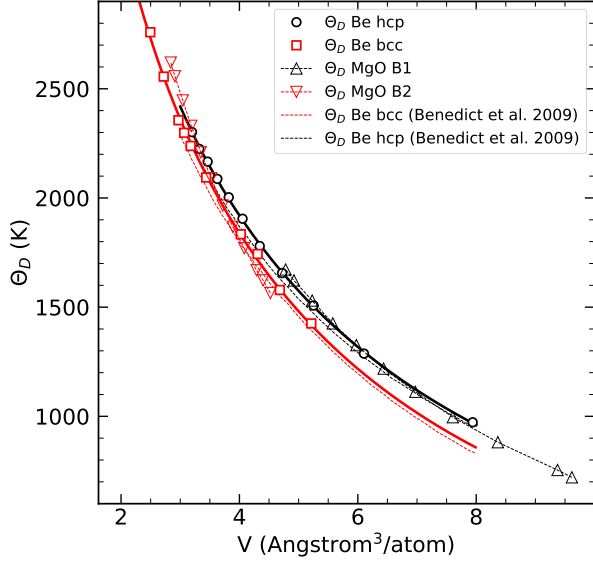
Figure 2. Logarithmic phonon moment (Debye temperature) of Be and MgO as function of volume per atom. The symbols represent results from individual harmonic calculations while lines are fit functions in form of Eq. (7).

Figure 3. Lindemann ratio, f, for two solid phases of MgO and Be. For a given pressure, all results were derived for the corresponding melting temperatures, T_m, that were obtained from the free energy calculations using the TDI method [17, 35]. The open symbols show results of the harmonic approximation in Eq. (5). The filled symbols correspond to average displacement, $\sqrt{\langle u^2 \rangle}$, computed along DFT-MD trajectories of Be in the respective phases, normalized by the nearest neighbor distance. **The green circles are results from an OCP model for Be that reproduce the harmonic calculations for the bcc phase quite well.**

which is obtained from integrating the phonon density of states, $g(\omega)$, of each phase. In Fig. 2, we plot the logarithmic moment of the two phases of Be and we fitted it to the functional form

$$\Theta_D(V) = \Theta_0(V^*) \left(\frac{V}{V^*} \right)^{-B} \exp\left[-A(V - V^*) \right], \quad (7)$$

as done in Refs. [30, 35]. We derived the fitting parameters $A = 0.086$ Å^{-1}, $B = 0.506$, $V^* = 6.085$ Å^3, and $\Theta_0(V^*) = 1299.00$ K for the hcp phase of Be and $A = 0.101$ Å^{-1}, $B = 0.515$, $V^* = 6.868$ Å^3, and $\Theta_0(V^*) = 1039.86$ K for bcc phase. We also observe that the logarithmic phonon moment of Be is very similar to that of MgO when compared at a given volume at either their low or high pressure phases. For MgO, the logarithmic phonon moment at zero-pressure is $\Theta_0^{\text{MgO}} = 720.71$ K, which is very close to the reported Debye temperature of $\Theta_D = 743$ K in experiments [75].

In Fig. 3, we plot the value of Lindemann's ratio, f, that we derived on the melting line with two different approaches. First, we derive Lindemann's ratio within the harmonic approximation. Using the fitted functions of Eq. (6) in Fig. 2, we derive the Debye temperature for a given pressure and then compute T_* to obtain the Lindemann's ratio from $f = \sqrt{T_m/T_*}$, where T_m is the melting temperature that we have obtained from our TDI calculations. This represents the right-hand side of Eq. (5). Second, we obtain the actual root mean squared displacement of the atoms, $\sqrt{\langle u^2 \rangle}$, that we observe in our simulations of solids at different melting points, and divide it by the nearest-neighbor distance, which corresponds to the left-hand
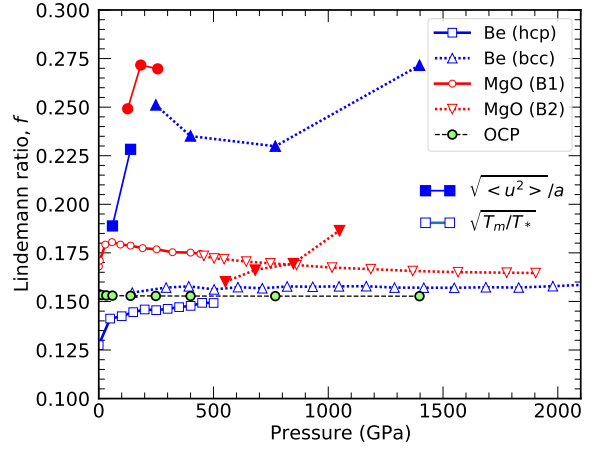
side of Eq. (5).

Since the nearest neighbor distance changes discontinuously between solid phases, one may not obtain a smooth curve for f, but one would expect it remains approximately constant along the melting line. Fig. 3 shows the value of f, obtained from the ratio between T_m and T_*, to be 0.13 for Be at $P = 0$ GPa, which is lower than for MgO, approximately 0.18. This means that atoms in the MgO crystal can withstand larger lattice vibrations than those in the Be crystal before melting sets in. In fact, as we will see in Section 3.4, at any given pressure, the phonon modes of Be have higher frequencies than those of MgO. According to the QHA, the Lindemann ratio of Be remains lower than that of MgO at high pressures, even after the phase transformation of both systems has taken place. We also observe that, as pressure increases, this factor f remains approximately constant (around 0.157) along the melting line for Be, while for MgO it shows a decreasing behavior with asymptotic convergence towards 0.165. This can be intuitively understood by recalling that, as the materials are compressed, the atoms come closer together and are subject to stronger repulsive forces, in line with the hypothesis presented by Hansen et al. [74].

However, when we compute the ratio f from the MSD values that we obtain from our DFT-MD simulations, we obtain values for f that are significantly higher than those predicted with harmonic theory. The normalization distance, a, was chosen

to be the nearest neighbor distance, but it can also be chosen as the lattice parameter at a given pressure. However, none of these choices allowed us to match the values calculated from the harmonic theory. We attribute this difference to the strong anharmonic effects at high temperature that are present in both materials. This discrepancy means that the Debye theory predicts rMSD values that can be up to 40% smaller than the actual displacements observed with DFT-MD simulation at the melting conditions. Estimating melting temperatures at high pressure from the ambient value of f would result in significant deviations from the actual melting temperature, because f changes with pressure.

For example, QHA predicts f to be 0.145 for the hcp phase of Be at 300 GPa while at ambient pressure, the value is only 0.130. If the ambient value had been used to infer the melting temperature at 300 GPa, it would have underestimated the melting temperature by 24% because f enters quadratically into Eq. (5). However, estimating the melting temperature of the B1 structure of MgO by consistently using the harmonic prediction value at ambient pressures works fairly well because the value of $f \approx 0.175$ remains approximately constant up to 1900 GPa, even after the transition to the B2 phase. Across this entire range, f varies by less than 8%, according to our estimations from the harmonic theory. Nevertheless, these values are not very useful to estimate the actual displacements that tend to be much larger than the harmonic predictions.

It is worth noticing that the differential Lindemann equation, which relates the slope of the melting curve to the Grüneisen parameter [76, 77], is much more effective in estimating the melting temperature than basing it on the Lindemann ratio, f [35].

Since beryllium is composed of only one type of ion, we also applied the one-component plasma (OCP) model to derive the Lindemann factor in the harmonic approximation. The OCP model approximates the ions in a real material by an ensemble of Coulomb charges in front of a rigid, neutralizing background of electrons [67, 68, 71, 72, 78]. At low temperature, the nuclei crystallize into a bcc lattice [67]. Following Refs. [68, 72], we derived the Lindemann factor for Be from the OCP model and added it to Fig. 3. We found good agreement between the OCP predictions and results that we derive with density functional theory that represents the forces on the nuclei more accurately. Both set of calculations relied on the harmonic approximation. The Lindemann ratio of the OCP model shows very little dependence on pressure and temperature and is approximately
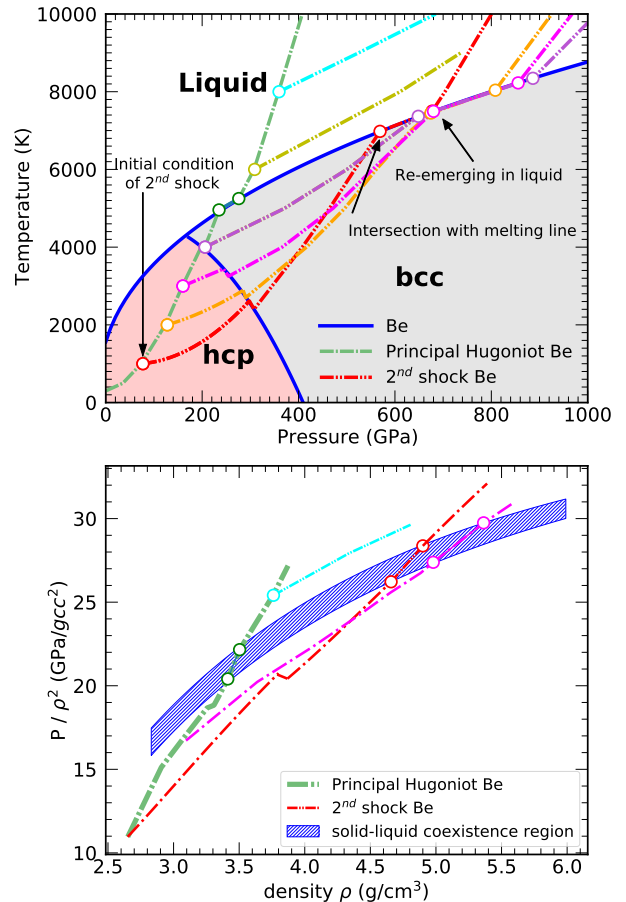

Figure 4. Phase diagram and shock Hugoniot curves of Be. The upper panels show how the principal and secondary shock Hugoniot curves shift at phase boundaries. The lower panels shows different Hugoniot curves as well as the solid-liquid-coexistence region in pressure-density space. For clarity, pressure on the Y axis has been divided by density squared.

15.3% [71, 72]. Our corresponding DFT results show slightly stronger dependence on pressure.

3.3. Shock Hugoniot Curves

In Fig. 4, we show the principal shock Hugoniot curve and a collection of double-shock Hugoniot curves of Be that we derived from our DFT-MD results. Double-shock experiments are designed to reach higher densities and lower temperatures than single-shock experiments. Recent double-shock experiments on MgO have reached pressures up to 2100 GPa [79]. However, diffraction measurements to determine the crystal structure and the onset of the B1-B2 phase transition have yet to be conducted. While no such experiments have been performed for Be, we provide a prediction here by generating several secondary shock Hugoniot curves based on our computed equation of state. Throughout this work, we employ the Rakine-

Hugoniot relation [80],

$$\tilde{H} = (E - E_0) + \frac{1}{2}(P + P_0)(V - V_0) = 0 \ , \qquad (8)$$

that relates the internal initial state energy, E_0, pressure, P_0, and volume, V_0 to the final shock energy, E, pressure, P and volume, V.

We predict that a second shock that starts from 77 GPa and 1000 K (**red dot-dashed line in Fig. 4**) on the principal Hugoniot curve, will intersect the hcp-bcc phase boundary at 300 GPa and 2400 K, then intersect the melting line at 570 GPa and 6980 K, and finally re-emerge at 680 GPa and 7500 K in the liquid phase. The gap between the solid and liquid branches along the melting is about $\sim$110 GPa, which represents a density change of 0.25 g cm^{-3}.

Fig. 4 shows that the slope in P-T space of the secondary shock Hugoniot curves is much shallower when they initially emerge from the principal Hugoniot curve, which means they intersect the hcp-bcc boundary and the melting line at much higher pressure than the principal Hugoniot curve. Eventually the slope of the secondary shock curves will steepen at much higher pressure but this range is outside of our consideration.

Fig. 4 illustrates that the offset between solid and liquid branches of the secondary Hugoniot curve is larger if the secondary Hugoniot curve starts from a higher pressure. For instance, if it starts from $P = 160$ GPa and $T = 3000$ K (**pink dot-dashed line in Fig. 4**), the secondary shock curve intersects the melting line at $\sim$680 GPa and enters the liquid phase only at $\sim$855 GPa, leaving a gap of 175 GPa, much wider than 40 GPa gap on the principal Hugoniot curve that started from ambient conditions.

Fig. 4 also shows that different secondary Hugoniot curves intersect one another, which is simply a consequence of shock compression curves converging to a compression ratio of 4 in the limit of high temperature. This means that secondary shock Hugoniot curves that start from a higher pressure and temperature have to intersect those that start at lower temperature and pressures.

Now we focus on the question how much the offset in pressure and temperature between liquid and solid branches of different secondary Hugoniot curve depends on their initial conditions. The magnitude of the offset is larger on the secondary Hugoniot curve than on the principal Hugoniot curve, and it increases if the starting point is chosen higher in pressure/temperature along the principal Hugoniot curve. To offer an explanation for both trends, we provide the following analytical arguments. The reason for the offset between the two branches lies in the differences between the EOS of the solid and the liquid, namely the enthalpy of fusion, ΔH and the difference

in specific volume, ΔV, for given P and T on the melting line. Introducing $E = H - PV$, we can rewrite Eq. (8) as,

$$2\tilde{H} = 2H - P(V + V_0) + P_0(V - V_0) - 2E_0 = 0 \ . \quad (9)$$

Then we consider EOS perturbations in enthalpy, dH, pressure, dP, and volume, dV, but require that the total differential, $d\tilde{H}$, remains zero to first order. Starting from the EOS point (H_S, P_S, V_S) where the solid Hugoniot branch intersects the melting line, we treat the switch to the closest liquid point on the Hugoniot $(H_L = \Delta H + H_S, P_L = \Delta P + P_S, V_L = \Delta V + V_S)$ as a perturbation to the EOS. This enables us to relate the offset in volume to the enthalpy of fusion, ΔH and a change in pressure, ΔP:

$$\frac{\Delta V}{V} \approx \frac{2\Delta H - \Delta P(V + V_0)}{(P - P_0)V} \ . \qquad (10)$$

We found that the two terms in the numerator, ΔH and $\Delta P(V + V_0)$, are of comparable magnitude and are thus both needed to determine the density offset between solid and liquid branches. More importantly, the denominator illustrates that with increasing P_0, the offset in volume between solid and liquid branches increases. This explains why the offset is small on the principal Hugoniot curve ($P_0 \approx 0$) and then increases for various secondary Hugoniot curves with rising P_0.

We found that the predictions of Eq. (10) agreed quantitatively fairly well with solving Eq. (8) explicitly for liquid and solid branches. For example, for the secondary Hugoniot curve that starts from 77 GPa and 1000 K (**red dashed curve in Fig. 4**), we calculated volume offset of $\Delta V/V = 4.1\%$ explicitly and while Eq. (10) predicts a change of 3.8%.

In Fig. 5, we show the principal and secondary shock Hugoniot curves of MgO. The gap in pressure on the melting line is much larger for secondary shock curves than it is on the principal Hugoniot curve and it widens with increasing starting pressure. This is the same trend we see for Be, which confirms our prediction based on Eq. (10).

In general we find that if a Hugoniot curve switches to a lower-density phase, like the liquid, it shifts to a higher pressure and temperature. Conversely if it switches into a slightly denser, solid phase, it shifts to a lower temperature but again to higher pressure. The temperature changes are a direct consequence of the Clapeyron slope, which is positive along the melting line but negative for the solid-solid transitions that we consider here.

It is interesting to note that the double shock is an interesting strategy to investigate the B2 phase as it allows to reach high pressures while keeping the temperatures moderate. For instance by exploring different starting points above 2000 K yet in the solid phase for the second shock, one can reach a large
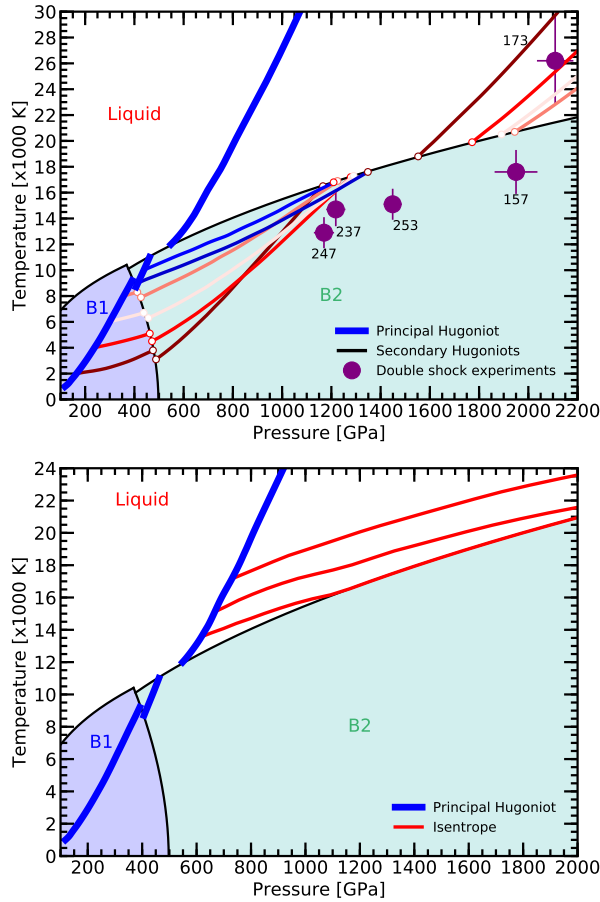
Figure 5. (Top) Principal and secondary shock Hugoniot curves of MgO are shown along with B1, B2, and liquid phases. The four lower secondary shock curves started in the B1 phase at 2000, 4000, 6000, and 8000 K, and respectively at 165, 238, 299, 356 GPa. The two upper curves begin in the B2 phase at 9000 and 10000 K. With increasing starting pressure, the gap widens between solid and liquid branches of the secondary curves as seen in Fig. 4. The filled circles represent results from recent double shock experiments [79]. The numbers nearby indicate the starting pressure of the second shock in GPa. (Bottom) Series of isentropes in liquid MgO started from the principal Hugoniot. These isentropes mimic a soft ramp compression [81] started after a first initial shock. The three different curves are for an entropy of 12, 12.5 and 13 k_{B}/atom from bottom to top.

portion of our predicted region of stability for B2, with pressures nearly as high as 1400 GPa. However states in the liquid phase at the same pressure and right above are actually unreachable with the same double shocks. As an example, if one were to investigate the liquid phase at 1200 GPa and 20,000 K, one would need to initiate the second shock already in the liquid phase.

In Fig. 5, we also compare our predictions with the recent double shock experiments by Hansen *et al.* [79]. Their secondary shocks started in the B1 phase from pressures between 157 and 253 GPa on the principal Hugoniot curve. Therefore only our two lowest double shock curves are relevant for a

comparison. We find that only the experimental data point at the highest pressure (2109 GPa) agrees with our DFT-MD results within error bars. Hansen *et al.* concluded that the three double-shock points from 1218−1950 GPa resided on the MgO melting line, which would imply a ∼10% lower melting temperature than we predicted with our DFT-MD simulations, a discrepancy of 2−3 σ. The largest deviation is seen for the experimental data point at 1950 GPa that started from 157 GPa on the principal Hugoniot curve because one needs to compare it with the brown double shock curve in which we predict to enter the liquid phase already at 1550 GPa. This means more work is needed to resolve these discrepancies, and that experimental and theoretical techniques have yet to agree on where the phase boundaries of MgO are located at megabar pressures.

We derived a set of isentropes initiated from the principal Hugoniot of MgO as can be seen in Fig. 5. They are an interesting way of exploring the liquid phase. For the lowest conditions reported in the figure, with an entropy of 12 k_{B}/atom, we predict that the isentrope intersects the melting line at circa 1100 GPa and 16,000 K and follows the melting line to at least 2000 GPa.

3.4. Phonon dispersion

The predicted phonon dispersion curves of the low-pressure phase of Be and MgO are shown in Fig. 6. We consider two volumes in each phase to show the effects of pressure. At 0 GPa, the phonon dispersion curves of Be and MgO show good agreement with previous calculations and experiments [33, 83, 84, 85].

We observe that for both materials, the phonon dispersion relations at high pressure are not connected with those at ambient pressure by a mere scaling factor, as both the acoustic and optic branches are qualitatively different. However, part of the topology is preserved, as splitting and merging of branches at the different points of the Brillouin zone show the same behavior. For example, the transverse optical branches that merge at the Γ point at 0 GPa around 14.5 THz, also merge at the Γ point at 400 GPa but at a much higher frequency of 24.4 THz for Be, and 40.9 THz for MgO. However, the ratio between frequencies of the longitudinal (LO) and transverse optical (TO) modes at the Γ point is much higher at high pressure (1.41 at 0 GPa vs. 2.10 at 400 GPa). At 0 GPa, the frequency of LO mode at the K point is higher than the frequency at the M point, but this feature is reversed at high pressure, where the frequency is higher at the M point compared to the K point. The gap between the acoustic branches at the M point also widens at high pressure.
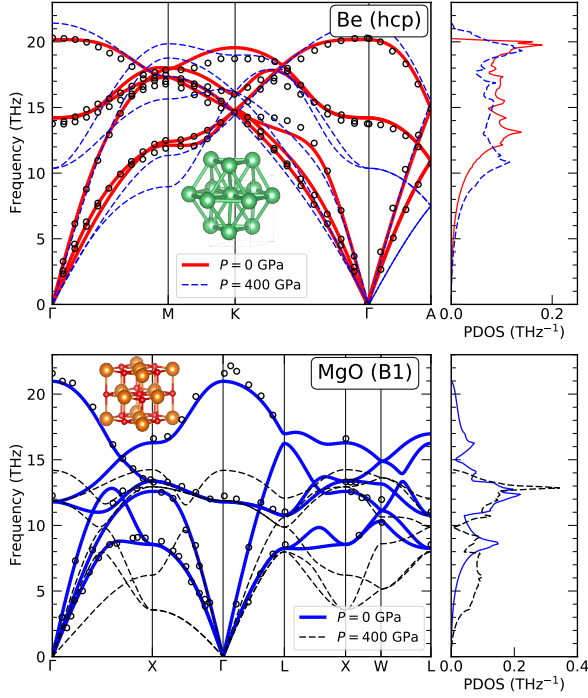
We also observe that the phonon dispersion

Figure 6. Phonon dispersion relations of Be and MgO in their low-pressure phases (hcp and B1, respectively). To illustrate how the phonon frequencies change with pressure within harmonic theory, we show results for 0 and 400 GPa. The corresponding densities are 1.88 and 4.32 $g\,cm^{-3}$ for Be, and 3.47 and 6.80 $g\,cm^{-3}$ for MgO. The respective phonon density of states is shown at the right. The higher frequencies at 400 GPa have been scaled by a factor of 0.42 for Be and by 0.35 for MgO to match the frequencies of the acoustic branch at the K point and the optical branch at the X point, respectively. All PDOS plots have been normalized to 1. The open circles represent experimental data at 0 GPa [82, 83, 84, 85].

relations of MgO in the B1 phase in Fig. 6 have many similarities to those of Be in the hcp phase. The highest frequency of ∼21 THz at the Γ point corresponds to the optical branch that emerges due to the LO-TO splitting caused by the dipolar moment interactions, which resembles the LO branch of Be. However, the shape of PDOS of MgO, unlike that of Be, changes significantly from 0 to 400 GPa. The disappearance of the low frequency peak in the PDOS of MgO and the sharp increase of the high frequency peak, followed by a rapid decrease to zero, indicates the stiffening of phonon modes of the B1 structure at 400 GPa, where the reduction of the LO-TO gap is smaller due to the reduction in strength of the dipole effect.

In Fig. 7, we show the evolution of the phonon density of states of Be and MgO in their low pressures phases (hcp and B1, respectively) as a function of the volume, which highlights how the low-frequency peak of the B1 phase of MgO decreases respect to the high-frequency peak. The PDOS of the hcp of Be shows a sharpening of the high-frequency peak with reducing
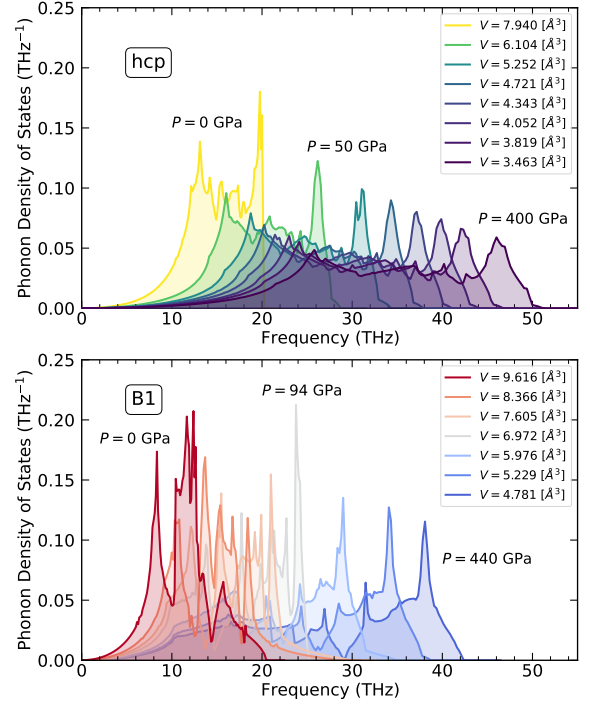
Figure 7. Progression of the phonon density of states of Be in the hcp structure and of MgO in the B1 phase are shown as function of frequency. The volumes per atom are given in the legend.

pressure and its spreading across a wider range of frequencies at high pressure. We can observe that the PDOS of Be is always non-zero at all frequencies, while the B1 phase of MgO has a local minimum that decreases to almost zero at high pressure. However, this pressure is close to the transition pressure, so we do not expect a gap to open in the PDOS of MgO in the B1 phase.

In Fig. 8, we compare the phonon dispersion relations of the high-pressure phases of MgO and Be. Contrary to what we observe for the low-pressure phases, the high-pressure phases of MgO and Be do not exhibit significant changes in the dispersion relations with respect pressure. The dispersion curves of the bcc and B2 phases of Be and MgO, respectively, are almost identical at the two pressures considered when they are scaled by a proper factor, where the lower pressure corresponds to the transition pressure at 0 K. The connections of the branches shows the same topology at 1904 GPa with respect to 500 GPa. This means, for example, that the ratio between the frequencies of the TO and LO branches at the Γ point is almost the same at low and high pressure. However, the presence of two types of atomic species in MgO still generates a gap in the B2 phase at the Γ point due to the LO-TO splitting, while this does not occur in the bcc phase of Be, despite the physical resemblance of the unit cells.
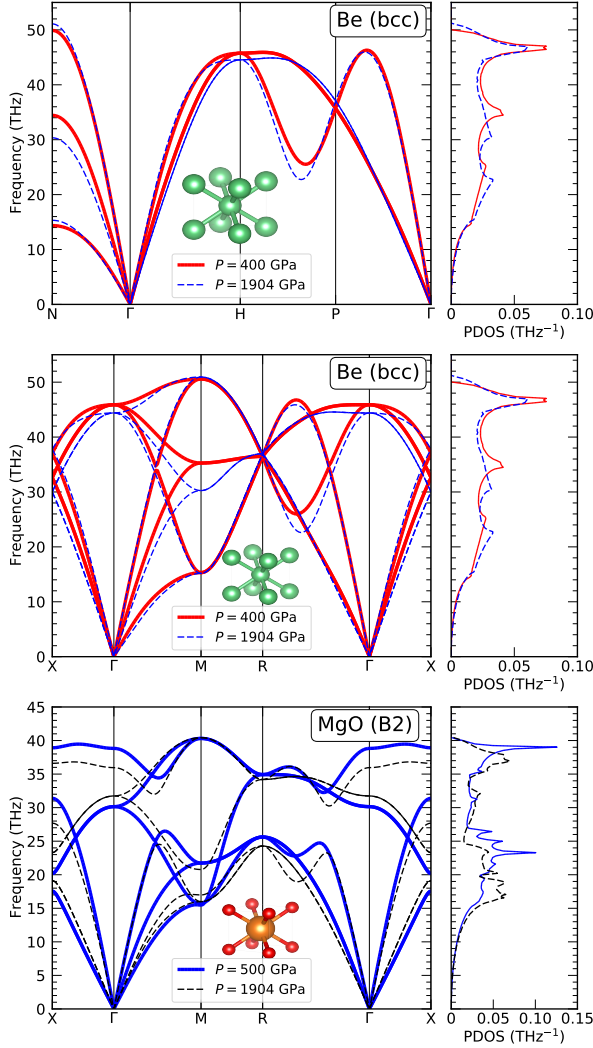
Figure 8. Phonon dispersion relations of the high-pressure phases of Be and MgO (bcc and B2, respectively) at two different pressures. The higher frequencies of Be at 1904 GPa have been scaled down by a factor of 0.58, while those of MgO at 1904 GPa, by a factor of 0.60. The X-Γ-M-R-Γ-X path for the unit cell of the bcc structure of Be is shown in the middle panel, so that it can be compared directly with the Brillouin zone of B2 structure of MgO. All PDOS have been normalized to 1.

3.5. Phonon quasiparticles and anharmonic effect

In order to quantitatively describe the anharmonic effects of Be and MgO, we derive phonon quasiparticles, fitting their peak and linewidth from our DFT-MD simulation trajectories [61, 62]. In order to quantify the anharmonic (excess) contribution to the vibrational Helmholtz free energy at a given density, we determine the excess entropy and internal energy to the Helmholtz free energy that results from anhamonic contributions, defined by

$$\Delta S = S_{\mathrm{qph}} - S_{\mathrm{QHA}}, \tag{11}$$

$$\Delta U = U_{\mathrm{DFT-MD}} - U_{\mathrm{QHA}} - U_0 \tag{12}$$

where ΔS stands for the excess entropy beyond QHA, which we obtained from the vibrational frequencies of our fitted phonon quasiparticles. ΔU represents the internal energy derived from our DFT-MD simulations and QHA calculations, and U_0 is the internal energy of the perfect lattice from static DFT calculations.

In our previous study [35], we found that the vibrational modes of the hcp phase of beryllium are softened significantly compared to the bcc phase at high temperatures, which increases the entropy and decreases the Helmholtz free energy, stabilizing the hcp phase. Thus, the transition pressures from the hcp to the bcc phase increase due to this anharmonic effect. When we derive the phonon quasi-particles for MgO, we find that the anhamonic contributions at high temperature make the entropic term, $-T\Delta S$, sharply decrease with temperature for the B1 phase, as we can see Fig. 9, making this low-pressure phase more stable at higher temperatures compared to QHA results. In contrast, the excess entropy (anharmonic) of B2 phase decreased with increasing temperature, which increases the overall Helmholtz free energy (see the red solid curve in Fig. 9). The vibration modes of B2 MgO on average become stiffer at high temperature with a free energy increase on a order of ~ 0.1 eV/atom, which is contrary to the behavior of B1 phase and accounts for the increase of B1-B2 transition temperature and triple point temperature. Our resulting free energy excess obtained via the phonon quasiparticle method are in a good agreement with the calculations carried out by Bouchet *et al.* [29] where they also predict that the $-TS$ term in Helmholtz free energy of the B1 phase decreases considerably with temperature, compensating the rise in internal energy. Conversely, the internal energy of the B2 phase remains approximately constant, while the $-TS$ term increases with temperature. We found the average frequency of B2 MgO to slightly increase with temperature. This is in agreement with the projection quasi-harmonic approximation (PQHA) method [17, 86] which also predicted a moderate stiffening effect of B2 MgO. This is also confirmed by the phonon density of state (PDOS) at T = 4000 K in Fig. 10 where the frequencies of B2 MgO are generally shifted to higher frequencies while the PDOS of B1 MgO to lower ones.

4. Conclusion

We systematically compared the phase diagrams of Be and MgO and provided a detailed characterization of the phonon band structures, assessing the anharmonic contributions via phonon quasiparticles and thermodynamic integration that allowed us to identify the source of the anharmonicity. We also derived
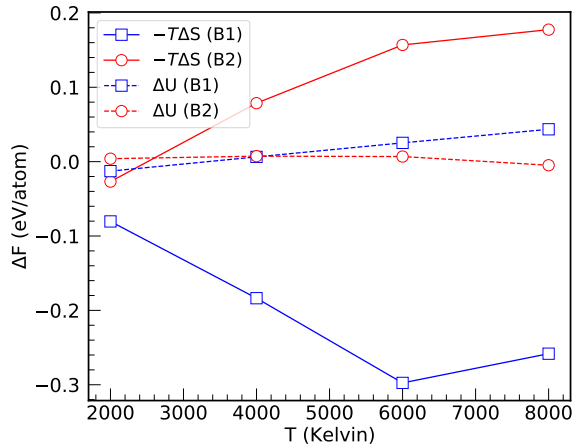
Figure 9. Anharmonic free energy of B1 and B2 phase of MgO compared at different temperatures at constant density ρ=6.83 g/cm^3. Solid lines: entropic contribution (fitted from phonon quasiparticles) to the anharmonic part of Helmholtz free energy; Dashed lines: energetic contribution of anharmonic helmholtz free energy. B1 and B2 phases are labelled with blue and red colors respectively.
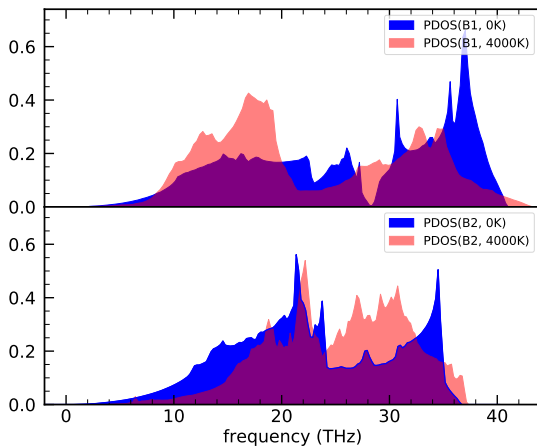

Figure 10. Phonon density of state (PDOS) of MgO at 0 K and 4000 K with fixed density $\rho = 6.83$ g/cm^3.

secondary shock Hugoniot curves and studied its relation to the melting line.

Both materials have very different bonding and electronic properties. Be is an electrical conductor governed by metallic bonding while magnesium oxide is an insulating, ionic material. Still both materials share many properties at megabar pressures: 1) With two solid phases separated by a line with a negative Clapeyron slope, their phase diagrams are similar. Anharmonic effects increase the stability field of the lower-pressure phase, which shifts the solid-solid-liquid triple point to higher pressures. 2) The principal shock Hugoniot curve remains predominantly in the lower-pressure solid phase but still enters the higher-pressure phase for a small pressure

interval just before melting. 3) There is a drop in temperature when a shock Hugoniot curve enters a denser solid phase. Conversely there is an increase in temperature and pressure upon melting. We found that the gap between solid and liquid branches of the secondary Hugoniot curve widens when the shock started from a higher initial pressure, P_0. Our secondary shock Hugoniot curves differed from the measurements by Hansen *et al.* and more work will be needed for experimental and theoretical methods to converge onto a single phase diagram for MgO.

We found that both versions of Lindemann's law to be unreliable to predict the melting of Be and MgO at megabar pressures. It assumes that on the melting line, the root-mean-squared displacement of the atoms is a constant fraction of the nearest-neighbor distance. However, we found this fraction to vary by up to 50% when we calculated it with molecular dynamics simulations that included anharmonic effects. When we calculated this fraction within the harmonic approximation, it did not vary nearly as much but still deviation of $10-20\%$ were identified.

Regarding the anharmonic contribution to the free energy of the solid phases, we found from either of our TDI or phonon quasiparticle calcualtions, that anharmonic effects help to stabilize the low-pressure phases of both materials, namely, hcp beryllium and B1 MgO, dominated by a large entropy source from softened vibrational modes. **We hope our research sheds lights on the research fields of material science and geoscience and possibly helps unveil universality laws of anharmonicity of more complex types of materials in the future.**

Acknowledgement

References

[1] Hemley R J 2000 *Annual Review of Physical Chemistry* **51** 763–800

[2] Mao H k and Hemley R J 1994 *Reviews of modern physics* **66** 671

[3] Mao H K, Chen X J, Ding Y, Li B and Wang L 2018 *Reviews of Modern Physics* **90** 015007

[4] Birch F 1952 *Journal of Geophysical Research* **57** 227–286

[5] Hazen R M and Jeanloz R 1984 *Reviews of Geophysics* **22** 37–46

[6] Jeanloz R and Morris S 1986 *Annual Review of Earth and Planetary Sciences* **14** 377–415

[7] Tsuchiya T, Tsuchiya J, Umemoto K and Wentzcovitch R M 2004 *Earth and Planetary Science Letters* **224** 241–248

[8] Tsuchiya T, Wentzcovitch R M, Da Silva C R and De Gironcoli S 2006 *Physical Review Letters* **96** 198501

[9] Hirose K, Labrosse S and Hernlund J 2013 *Annual Review of Earth and Planetary Sciences* **41** 657–691

[10] Wahl S M, Hubbard W B, Militzer B, Guillot T, Miguel Y, Movshovitz N, Kaspi Y, Helled R, Reese D, Galanti E et al. 2017 *Geophysical Research Letters* **44** 4649–4659

[11] Coppari F, Smith R, Eggert J, Wang J, Rygg J, Lazicki A, Hawreliak J, Collins G and Duffy T 2013 *Nature Geoscience* **6** 926–929

[12] Mao H and Bell P 1979 *Journal of Geophysical Research: Solid Earth* **84** 4533–4536

[13] Zha C S, Mao H k and Hemley R J 2000 *Proceedings of the National Academy of Sciences* **97** 13494–13499

[14] Dorogokupets P I and Oganov A R 2007 *Physical Review B* **75** 024115

[15] Wilson I 1981 *IEE Proceedings A (Physical Science, Measurement and Instrumentation, Management and Education, Reviews)* **128** 159–164

[16] Shand M A 2006 *The chemistry and technology of magnesia* (John Wiley & Sons)

[17] Soubiran F and Militzer B 2020 *Physical Review Letters* **125** 175701 ISSN 0031-9007 URL https://doi.org/10.1103/PhysRevLett.125.175701https://link.aps.org/doi/10.1103/PhysRevLett.125.175701

[18] Duffy T S, Hemley R J and Mao H k 1995 *Physical Review Letters* **74** 1371

[19] Guillot T 2005 *Annu. Rev. Earth Planet. Sci.* **33** 493–530

[20] Wilson H F and Militzer B 2012 *Physical Review Letters* **108** 111101

[21] Feinberg L D, Clampin M, Keski-Kuha R, Atkinson C, Texter S, Bergeland M and Gallagher B B 2012 James webb space telescope optical telescope element mirror development history and results *Space Telescopes and Instrumentation 2012: Optical, Infrared, and Millimeter Wave* vol 8442 (International Society for Optics and Photonics) p 84422B

[22] Stinton G W, Macleod S G, Cynn H, Errandonea D, Evans W J, Proctor J E, Meng Y and McMahon M I 2014 *Physical Review B - Condensed Matter and Materials Physics* **90** 1–7 ISSN 1550235X

[23] Belonoshko A B, Arapan S, Martonak R and Rosengren A 2010 *Physical Review B* **81** 054110 ISSN 1098-0121 URL http://link.aps.org/doi/10.1103/PhysRevB.81.054110https://link.aps.org/doi/10.1103/PhysRevB.81.054110

[24] Boates B and Bonev S A 2013 *Physical Review Letters* **110** 1–5 ISSN 00319007

[25] Cebulla D and Redmer R 2014 *Physical Review B - Condensed Matter and Materials Physics* **89** 1–10 ISSN 1550235X

[26] Root S, Shulenburger L, Lemke R W, Dolan D H, Mattsson T R and Desjarlais M P 2015 *Physical Review Letters* **115** 1–6 ISSN 10797114

[27] Miyanishi K, Tange Y, Ozaki N, Kimura T, Sano T, Sakawa Y, Tsuchiya T and Kodama R 2015 *Physical Review E* **92** 023103

[28] Taniuchi T and Tsuchiya T 2018 *Journal of Physics Condensed Matter* **30** ISSN 1361648X

[29] Bouchet J, Bottin F, Recoules V, Remus F, Morard G, Bolis R M and Benuzzi-Mounaix A 2019 *Physical Review B - Condensed Matter and Materials Physics* **99** 094113 ISSN 2469-9950 URL https://link.aps.org/doi/10.1103/PhysRevB.99.094113

[30] Benedict L X, Ogitsu T, Trave A, Wu C J, Sterne P A and Schwegler E 2009 *Physical Review B - Condensed Matter and Materials Physics* **79** 1–9 ISSN 10980121

[31] Robert G, Legrand P and Bernard S 2010 *Physical Review B* **82** 104118 ISSN 1098-0121 URL https://link.aps.org/doi/10.1103/PhysRevB.82.104118

[32] Luo F, Cai L C, Chen X R, Jing F Q and Alf D 2012 *Journal of Applied Physics* **111** ISSN 00218979

[33] Xian J W, Yan J, Liu H F, Sun T, Zhang G M, Gao X Y and Song H F 2019 *Physical Review B* **99** 1–12 ISSN 24699969

[34] Wu C J, Myint P C, Pask J E, Prisbrey C J, Correa A A, Suryanarayana P and Varley J B 2021 *The Journal of Physical Chemistry A* **125** 1610–1636

[35] Wu J, González-Cataldo F and Militzer B 2021 *Physical Review B* **104** 014103 ISSN 2469-9950 URL https://link.aps.org/doi/10.1103/PhysRevB.104.014103

[36] Lazicki A, Dewaele A, Loubeyre P and Mezouar M 2012 *Physical Review B - Condensed Matter and Materials Physics* **86** 1–10 ISSN 10980121

[37] McCoy C A, Knudson M D and Desjarlais M P 2019 *Physical Review B* **100** 1–13 ISSN 24699969

[38] Kresse G and Furthmüller J 1996 *Computational Materials Science* **6** 15–50 ISSN 09270256

[39] Blöchl P E 1994 *Phys. Rev. B* **50**(24) 17953–17979 URL https://link.aps.org/doi/10.1103/PhysRevB.50.17953

[40] Kresse G and Joubert D 1999 *Physical Review B* **59** 1758–1775 ISSN 0163-1829 URL https://link.aps.org/doi/10.1103/PhysRevB.59.1758

[41] Nosé S 1984 *The Journal of Chemical Physics* **81** 511–519 ISSN 00219606

[42] Nosé S 1991 *Progress of Theoretical Physics Supplement* 1–46

[43] Mermin N D 1965 *Physical Review* **137** A1441

[44] Perdew J P, Burke K and Ernzerhof M 1996 *Physical Review Letters* **77** 3865–3868 ISSN 0031-9007 URL https://link.aps.org/doi/10.1103/PhysRevLett.77.3865

[45] González-Cataldo F, Soubiran F and Militzer B 2020 *Physics of Plasmas* **27** 092706 ISSN 1070-664X (*Preprint* 2008.08459) URL http://aip.scitation.org/doi/10.1063/5.0017555http://arxiv.org/abs/2008.08459

[46] Driver K P, Soubiran F, Zhang S and Militzer B 2015 *The Journal of Chemical Physics* **143** 164507 ISSN 0021-9606 URL http://scitation.aip.org/content/aip/journal/jcp/143/16/10.1063/1.4934348

[47] Allen M and Tildesley D 1987 *Computer Simulation of Liquids* (Oxford: Clarendon Pr)

[48] Flyvbjerg H and Petersen H G 1989 *The Journal of Chemical Physics* **91** 461–466

[49] Monkhorst H J and Pack J D 1976 *Physical Review B* **13** 5188–5192 ISSN 0556-2805 URL https://link.aps.org/doi/10.1103/PhysRevB.16.1748https://link.aps.org/doi/10.1103/PhysRevB.13.5188

[50] Frenkel D and Ladd A J C 1984 *The Journal of Chemical Physics* **81** 3188–3193 ISSN 0021-9606 URL http://aip.scitation.org/doi/10.1063/1.448024

[51] de Wijs G A, Kresse G and Gillan M J 1998 *Physical Review B - Condensed Matter and Materials Physics* **57** 8223–8234 ISSN 1550235X

[52] Polson J M, Trizac E, Pronk S and Frenkel D 2000 *Journal of Chemical Physics* **112** 5339–5342 ISSN 00219606

[53] Navascués G and Velasco E 2010 *The Journal of Chemical Physics* **132** 134106 ISSN 0021-9606 URL http://aip.scitation.org/doi/10.1063/1.3372805

[54] Izvekov S, Parrinello M, Bumham C J and Voth G A 2004 *Journal of Chemical Physics* **120** 10896–10913 ISSN 00219606

[55] Wahl S M, Wilson H F and Militzer B 2013 *The Astrophysical Journal* **773** 95

[56] Wilson H F and Militzer B 2010 *Phys. Rev. Lett.* **104**(12) 121101 URL https://link.aps.org/doi/10.1103/PhysRevLett.104.121101

[57] González-Cataldo F, Wilson H F and Militzer B 2014 *The Astrophysical Journal* **787** 79

[58] Frenkel D and Smit B 2001 *Understanding molecular*

simulation: from algorithms to applications vol 1 (Elsevier)

[59] Baroni S, De Gironcoli S, Dal Corso A and Giannozzi P 2001 *Reviews of modern Physics* **73** 515

[60] Togo A and Tanaka I 2015 *Scr. Mater.* **108** 1–5

[61] Carreras A, Togo A and Tanaka I 2017 *Computer Physics Communications* **221** 221–234

[62] Zhang D B, Sun T and Wentzcovitch R M 2014 *Physical review letters* **112** 058501

[63] Wallace D C 1972 *American Journal of Physics* **40** 1718–1719

[64] Coppari F, Smith R F, Wang J, Millot M, Kim D, Rygg J R, Hamel S, Eggert J H and Duffy T S 2021 *Nature Geoscience* **14** 121–126 ISSN 1752-0894 URL http://dx.doi.org/10.1038/s41561-020-00684-yhttp://www.nature.com/articles/s41561-020-00684-y

[65] Stixrude L 2012 *Physical Review Letters* **108** 055505 ISSN 0031-9007 URL http://link.aps.org/doi/10.1103/PhysRevLett.108.055505

[66] González-Cataldo F, Davis S and Gutiérrez G 2016 Z method calculations to determine the melting curve of silica at high pressures *Journal of Physics: Conference Series* vol 720 p 012032 ISSN 1742-6588 URL http://stacks.iop.org/1742-6596/720/i=1/a=012032?key=crossref.a3072f95bd2993362255c11123cf08fd

[67] Pollock E L and Hansen J P 1973 *Physical Review A* **8** 3110

[68] Mochkovitch R and Hansen J 1979 *Physics Letters A* **73** 35–38

[69] Pines D 2018 *Elementary excitations in solids* (CRC Press)

[70] Wolf G H and Jeanloz R 1984 *Journal of Geophysical Research: Solid Earth* **89** 7821–7835

[71] Chabrier G, Ashcroft N and DeWitt H 1992 *Nature* **360** 48–50

[72] Chabrier G 1993 *The Astrophysical Journal* **414** 695–700

[73] Militzer B and Graham R L 2006 *Journal of Physics and Chemistry of Solids* **67** 2136–2143 ISSN 00223697 URL https://linkinghub.elsevier.com/retrieve/pii/S0022369706003088

[74] Hansen J P 1970 *Physical Review A* **2** 221

[75] Beg M 1976 *Acta Crystallographica Section A: Crystal Physics, Diffraction, Theoretical and General Crystallography* **32** 154–156

[76] Gilvarry J J 1956 *Physical Review* **102** 308

[77] Poirier J P 1989 *Physics of the earth and planetary interiors* **54** 364–369

[78] Militzer B and Graham R L 2006 *Journal of Physics and Chemistry of Solids* **67** 2136

[79] Hansen L E, Fratanduono D E, Zhang S, Hicks D G, Suer T, Sprowal Z K, Huff M F, Gong X, Henderson B J, Polsin D N, Zaghoo M, Hu S X, Collins G W and Rygg J R 2021 *Physical Review B* **104** 014106 ISSN 2469-9950 URL https://link.aps.org/doi/10.1103/PhysRevB.104.014106

[80] Zeldovich Y B, Raizer Y P, Hayes W and Probstein R 1967 *Physics of shock waves and high-temperature hydrodynamic phenomena. Vol. 2* (Academic Press New York)

[81] González-Cataldo F, Godwal B K, Driver K, Jeanloz R and Militzer B 2021 *Physical Review B* **104** 134104 ISSN 2469-9950 URL https://link.aps.org/doi/10.1103/PhysRevB.104.134104

[82] Stedman R, Amilius Z, Pauli R and Sundin O 1976 *Journal of Physics F: Metal Physics* **6** 157–166 ISSN 0305-4608 URL https://iopscience.iop.org/article/10.1088/0305-4608/6/2/012

[83] Peckham G 1967 *Proceedings of the Physical Society (1958-1967)* **90** 657

[84] Sangster M, Peckham G and Saunderson D 1970 *Journal of Physics C: Solid State Physics* **3** 1026

[85] Oganov A, Gillan M J and Price G D 2003 *Journal of Chemical Physics* **118** 10174–10182 ISSN 00219606

[86] Henry A S and Chen G 2008 *Journal of Computational and Theoretical Nanoscience* **5** 141–152